Journal of Physics: Condensed Matter

PAPER • OPEN ACCESS

Effect of Rashba and Dresselhaus spin–orbit coupling on supercurrent rectification and magnetochiral anisotropy of ballistic Josephson junctions

To cite this article: C Baumgartner *et al* 2022 *J. Phys.: Condens. Matter* **34** 154005

View the article online for updates and enhancements.

You may also like

- Elymat Measurement of Intentionally Contaminated and Dry Etched Wafers
J. Wittmann, W. Bergholz and H. Hoffmann
- Phonons in low-dimensional systems
A P Mayer, D Bonart and D Strauch
- Iron and Its Detrimental Impact on the Nucleation and Growth of Oxygen Precipitates during Internal Gettering Processes
B. Hackl, K. J. Range, H. J. Gores et al.

IOP ebooks™

Bringing together innovative digital publishing with leading authors from the global scientific community.

Start exploring the collection–download the first chapter of every title for free.

This content was downloaded from IP address 128.210.107.129 on 18/02/2022 at 19:00

OPEN ACCESS
IOP Publishing

Journal of Physics: Condensed Matter

J. Phys.: Condens. Matter **34** (2022) 154005 (10pp)

https://doi.org/10.1088/1361-648X/ac4d5e

Effect of Rashba and Dresselhaus spin–orbit coupling on supercurrent rectification and magnetochiral anisotropy of ballistic Josephson junctions

C Baumgartner[1], L Fuchs[1], A Costa[2], Jordi Picó-Cortés[2], S Reinhardt[1], S Gronin[3,4], G C Gardner[3,4], T Lindemann[4,5], M J Manfra[3,4,5,6,7], P E Faria Junior[2], D Kochan[2], J Fabian[2], N Paradiso[1,*] and C Strunk[1]

[1] Institut für Experimentelle und Angewandte Physik, University of Regensburg, 93040 Regensburg, Germany
[2] Institut für Theoretische Physik, University of Regensburg, 93040 Regensburg, Germany
[3] Microsoft Quantum Purdue, Purdue University, West Lafayette, Indiana 47907 United States of America
[4] Birck Nanotechnology Center, Purdue University, West Lafayette, Indiana 47907 United States of America
[5] Department of Physics and Astronomy, Purdue University, West Lafayette, Indiana 47907 United States of America
[6] School of Materials Engineering, Purdue University, West Lafayette, Indiana 47907 United States of America
[7] School of Electrical and Computer Engineering, Purdue University, West Lafayette, Indiana 47907 United States of America

E-mail: nicola.paradiso@physik.uni-regensburg.de

Received 1 December 2021, revised 12 January 2022
Accepted for publication 20 January 2022
Published 10 February 2022

Abstract

Simultaneous breaking of inversion- and time-reversal symmetry in Josephson junction (JJ) leads to a possible violation of the $I(\varphi) = -I(-\varphi)$ equality for the current–phase relation. This is known as anomalous Josephson effect and it produces a phase shift φ_0 in sinusoidal current–phase relations. In ballistic JJs with non-sinusoidal current phase relation the observed phenomenology is much richer, including the supercurrent diode effect and the magnetochiral anisotropy (MCA) of Josephson inductance. In this work, we present measurements of both effects on arrays of JJs defined on epitaxial Al/InAs heterostructures. We show that the orientation of the current with respect to the lattice affects the MCA, possibly as the result of a finite Dresselhaus component. In addition, we show that the two-fold symmetry of the Josephson inductance reflects in the activation energy for phase slips.

* Author to whom any correspondence should be addressed.

Original content from this work may be used under the terms of the Creative Commons Attribution 4.0 licence. Any further distribution of this work must maintain attribution to the author(s) and the title of the work, journal citation and DOI.

 © 2022 The Author(s). Published by IOP Publishing Ltd

Keywords: Rashba, Dresselhaus, supercurrent diode, magnetochiral anisotropy, nonreciprocal transport, epitaxial aluminum, superconducting 2DEG

(Some figures may appear in colour only in the online journal)

Charge transport in superconductors is driven by the phase gradient of the condensate wavefunction. In the exemplary case of Josephson junctions (JJs), this leads to a well-defined current–phase relation (CPR), which describes how the current I depends on the phase difference φ between the leads [1]. The CPR critically depends on the symmetries of the system: in particular *either* time-reversal *or* parity symmetry require that $I(\varphi) = -I(-\varphi)$. As a consequence, $I(0) = 0$ and the CPR can be written as a Fourier series of sine terms only, $I = \sum_n b_n \sin(n\varphi)$. If the temperature is close to the critical temperature T_c, or if the junction is relatively opaque (tunnel limit), then the CPR reduces to a sinusoidal relation, $I = I_0 \sin\varphi$.

To obtain a finite current at zero phase (and vice versa) it is necessary to break the equivalence between the leads (given by the space inversion symmetry) and simultaneously the time-reversal symmetry. This is called the anomalous Josephson effect [2–8]. The effect is possible in noncentrosymmetric superconductors with large spin–orbit interaction (SOI) in the presence of a magnetic field. In such systems theory predicts the possibility to have $I(\varphi) \neq -I(-\varphi)$. In the case of a sinusoidal CPR, this is equivalent to a finite phase offset φ_0, so that $I = I_0 \sin(\varphi + \varphi_0)$. Such φ_0-junctions have been experimentally demonstrated in several systems [9–12].

Noncentrosymmetric superconductors in a magnetic field also show magnetochiral anisotropy (MCA) effects, which arise when certain physical quantities display correction terms linear both in current and magnetic field [13–19]. The first quantity to display MCA is the resistance in the fluctuation regime of a superconductor near T_c [20–26]. In a recent work [27], we have found that the kinetic inductance of a superconductor as well shows the MCA effect. For JJs this means that the Josephson inductance L can be written as

$$L = L_0[1 + \gamma_L \hat{e}_z(\vec{B} \times \vec{I})], \quad (1)$$

where γ_L is the MCA coefficient for the inductance. As a consequence of the MCA, the critical currents for the two directions of the supercurrent flow differ, leading to a finite current interval where the resistance is zero only for one bias polarity. This is a supercurrent diode effect (first envisioned in reference [28]), which has been first demonstrated in bulk superconductors [29] and then in JJs [27]. In both cases, the SOI was of Rashba-type and the supercurrent rectification driven by the in-plane field perpendicular to the current. Very recent reports [30, 31] have demonstrated the supercurrent diode effect in systems with valley-Zeeman SOI (where the rectification is driven by the out-of-plane field, as expected from theory [32]), in type II Dirac semimetal [33], or in magic-angle twisted bilayer [34] or trilayer [35, 36] graphene. In turn, such intriguing experimental evidences have stimulated a number of theoretical studies on non-reciprocal supercurrent in exotic systems [36–42]. As discussed in our previous work [27], in JJs with Rashba SOI, the supercurrent diode effect is strictly related to the φ_0 shift discussed above. The MCA and supercurrent diode generalize the anomalous Josephson effect to the case of nonsinusoidal (i.e., skewed) CPRs.

In this work, we study the supercurrent diode effect and the MCA in JJ arrays with large Rashba SOI. We present experiments that complement the main observations reported in reference [27]: we show results for different lattice orientations, which we use to estimate the Dresselhaus contribution to the SOI; we study the MCA for the activation energy of thermally activated phase slips, which we connect to the anisotropy of the inductance. Our results provide a useful illustration of the role of SOI on the CPR.

1. Ballistic SNS junctions in epitaxial AL/InAs heterostructures

A clean superconductor with synthetic Rashba interaction can be produced combining an epitaxial Al film and a high-mobility 2D electron gas (2DEG) confined in a InGaAs/InAs quantum well. If the barrier between 2DEG and Al film is transparent, then the 2DEG former will be proximitized by the superconducting Al, leading to a Rashba 2D superconductor. The combination of superconductivity and SOI is at the basis of topological superconductivity. This material platform has therefore been mainly developed by the community studying Majorana modes and topological superconductivity.

Our devices are fabricated starting from a heterostructure whose top layers are Al (7 nm)/$In_{0.2}Ga_{0.8}As$ (10 nm)/InAs (2DEG) (7 nm)/$In_{0.2}Ga_{0.8}As$ (4 nm) (see the supplementary material of reference [43] for the full layer sequence). To obtain JJs of finite width W we define a mesa using a phosphoric acid-based wet etching procedure. The chosen width W is the result of a compromise between a sufficiently high Josephson coupling (increasing with W) and a measurable Josephson inductance (decreasing with W). In our experiments this leads to widths of the order of few micrometers, which correspond to a critical current of several microamperes.

SNS junctions are obtained by selectively etching Al to form 100 nm-long gaps separating the remaining rectangular Al islands. A SEM picture of the device is shown in figure 1(a), while a sketch of it is depicted in figures 1(b) and (c). The selective etching is by far the most critical step of the fabrication process. The disorder introduced into the shallow 2DEG of the exposed InAs regions must be minimized in order to obtain ballistic junctions with high transparency.

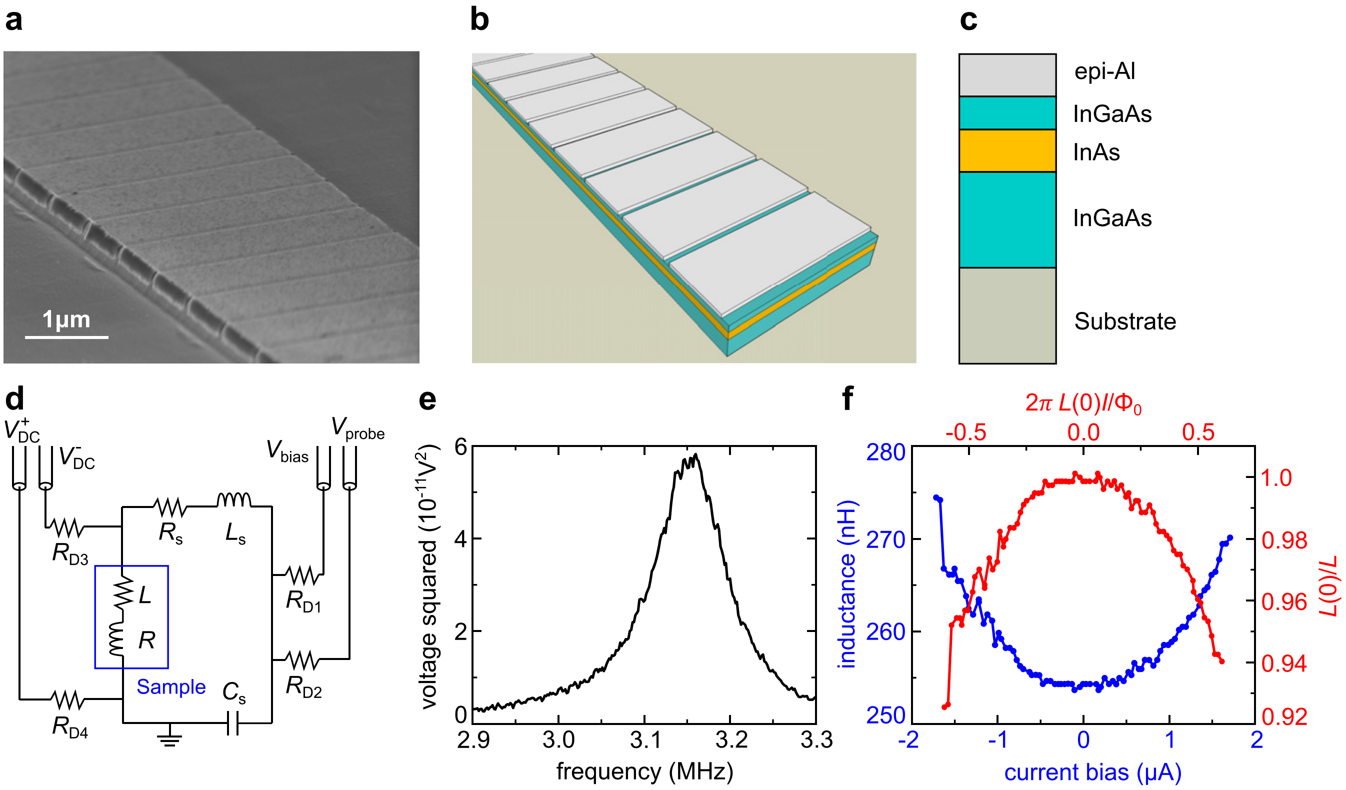

Figure 1. (a) Scanning electron micrograph of a portion of the Josephson junction arrays under study (sample 3). The 3.3 μm-wide mesa is fabricated by deep etching, while the gaps between the top Al islands are obtained by selective etching. (b) Corresponding scheme of the structure. The yellow part highlights the quantum well where the 2D electron gas is located. (c) Top layer sequence for the heterostructure. As substrate, we indicate the remaining layers, not relevant for the transport. The complete sequence can be found in reference [43]. (d) Scheme of the cold RLC circuit located next to the sample. (e) Resonance curve measured for sample 3 at T =100 mK, and at zero applied DC bias and field. (f) Measured $L(I)$ curve for the same sample. Each L value is deduced from the center frequency of the corresponding RLC resonance spectrum.

2. Cold RLC resonators for Josephson inductance measurements in the MHz regime

DC transport measurements provide only partial information about single JJs. For instance, the Josephson coupling between the leads is deduced from the critical current—an interesting situation where an *equilibrium* quantity is deduced from AC transport measurements. The CPR is not accessible without making use of a SQUID geometry in perpendicular magnetic field. Josephson coupling and CPR can instead be directly accessed in single junctions by measuring its Josephson inductance, clearly with AC measurements. For example, given the CPR relation$I = I_0 f(\varphi)$ (where I_0 is the relevant current scale and f is a 2π periodic function) the Josephson inductance immediately emerges from the ratio between Josephson voltage and time derivative of the CPR

$$L(\varphi) = \frac{V}{\frac{\mathrm{d}}{\mathrm{d}t}I} = \frac{\Phi_0 \frac{\mathrm{d}\varphi}{\mathrm{d}t}\frac{1}{2\pi}}{\frac{\mathrm{d}}{\mathrm{d}t}[I_0 f(\varphi)]} = \frac{\Phi_0}{2\pi I_0 f'(\varphi)}. \tag{2}$$

In a simple junction without loop, it is the current and not the phase that is controlled, therefore it is convenient to integrate $\dot{\varphi} = 2\pi L\dot{I}/\Phi_0$ to obtain the inverse CPR $\varphi(I)$:

$$\varphi(I) - \varphi(0) = \frac{2\pi}{\Phi_0}\int_0^I L(I')\mathrm{d}I', \tag{3}$$

where $L(I)$ is the measured quantity. Therefore, the Josephson inductance as a function of the current is proportional to the derivative of the inverse CPR $\varphi(I)$.

The difficulties in the measurement of the Josephson inductance are related to the fact that it is typically much smaller than the inductance of the cryostat cables. To decouple the sample from the external cabling, it is possible to embed the sample in a low resistance resonator decoupled from the external leads by resistors. The resonance frequency will then directly provide the inductance if the Q factor is above unity. The circuit scheme of the RLC resonator used in this work is shown in figure 1(d). The Q factor of the loop is approximately given by the formula for series RLC tank, $Q = \frac{1}{R_l}\sqrt{\frac{L_l}{C_s}}$. Here R_l and L_l are, respectively, the total resistance (i.e., sample resistance R plus external circuit resistance in series R_s) and total inductance of the loop (i.e., sample inductance L plus external circuit inductance in series L_s), while C_s is the series capacitance, given by an external capacitor. The choice of the working point for the frequency is crucial. For a series RLC, the higher the frequency, the higher the sensitivity. On the other hand, at very high frequency measurements in the presence of magnetic fields are difficult since emerging dissipation would immediately damp the resonance. Moreover, at high frequency (rf regime close to the plasma frequency) the physics of a JJ is not equivalent to that in DC. At very high frequency, one must take into account transmission line resonance on the very sample.

For our measurements we have chosen to operate in the MHz range. This frequency regime allows us to operate under large magnetic fields without significant damping of the resonance. Also, this frequency range is below any relevant physical threshold for the JJs under study (plasma frequency $\omega_P \approx 240$ GHz, first transmission line mode for the array $\omega_0 = 250$ MHz), so that for any practical purpose we are operating in quasi-DC regime. Figure 1(e) shows a typical resonance spectrum measured by lock-in, whose center frequency directly provides the inductance. The Josephson inductance is obtained by subtracting the external inductance of the circuit, which has been determined in a dedicated calibration session. Our typical inductance measurement consists in measuring RLC spectra as a function of control parameters, e.g., the DC current as in the measurement of $L(I)$ shown in figure 1(f). The inductance is deduced from the resonance frequency, since the external resistance R_s, capacitance C_s and inductance L_s in series to the sample [see circuit scheme in figure 1(d)] are known.

This method (which is an adaptation, with modern electronics, of the experiment in reference [44]) makes it also possible to accurately extract the sample resistance R via the resonance quality factor Q. However, for our circuit parameter, the Q factor is suppressed already for resistances of the order of 1 Ω, which is roughly four orders of magnitude less than the normal resistance of our samples. This means that the inductance measurements shown here are all conducted deep in the superconducting regime, where the resistance is a very small fraction of the normal state resistance.

As shown below, the typical inductance of a 3 μm-wide and 100 nm-long JJ is of the order of 100 pH. In the MHz regime we operate in, this inductance is below the resolution limit of our electronics. Therefore, instead of a single junction, we measure an array of thousands junctions. If their spacing is sufficient to exclude mutual (e.g., magnetic) interaction, they will behave as a set of inductors in series, i.e., the measured inductance will reflect the sum of the ensemble. This configuration has advantages and disadvantages. The disadvantage is that the critical current (or field) is set by the weakest junction. When that value is reached the emerging resistance is enough to damp the resonance. For this reason, measured $L(I)$ curves, as e.g. that shown in figure 1(f), terminate before the expected divergence at the critical current. Working with arrays has also crucial advantages beyond the obvious increase in sensitivity. In fact, in large JJ arrays imperfections in single JJs are unimportant, since only the average behavior is measured. If a weaker junction is present, its inductance will be higher than the typical one, but it will hardly affect the total inductance given by thousands of JJs. This is true as long as the current is below the reduced critical current value for the weakest junction, as discussed above.

3. Characterization of ballistic Josephson junctions in Rashba 2DEGs

The CPR of short ballistic SNS junctions at finite temperature T can be described by the complete Furusaki–Beenakker formula [45, 46]

$$I(\varphi) = I_0 f(\varphi) = I_0 \frac{\bar{\tau}\,\sin\varphi\,\tanh\left[\frac{\Delta^*}{2k_B T}\sqrt{1-\bar{\tau}\sin^2\left(\frac{\varphi}{2}\right)}\right]}{2\sqrt{1-\bar{\tau}\sin^2\left(\frac{\varphi}{2}\right)}}, \tag{4}$$

where $\bar{\tau}$ it the transmission coefficient and Δ^* is the effective gap at the leads. In our case $\bar{\tau}$ refers to the *average* transmission coefficient, while Δ^* refers to the induced gap in the 2DEG region just underneath the epitaxial Al film. The characteristic current I_0 (which coincides with the critical current only for $\bar{\tau} \to 1$ and $T \to 0$) is given by

$$I_0 = \frac{e\Delta^*}{\hbar} N, \tag{5}$$

where N is the number of spin-degenerate transverse modes in the channel. To characterize our junctions we need three parameters, namely I_0,$\bar{\tau}$ and Δ^*. The first two can be obtained from a $L(I)$ measurement at $T/T_c \ll 1$. In particular, $\bar{\tau}$ is determined from the curvature of the graph of $L(0)/L$ versus $2\pi L(0)I/\Phi_0$, which in the low temperature limit depends only on $\bar{\tau}$ [43], see red curve in figure 1(f).

The transmission coefficient strictly depends on the quality of the selective Al etching defining the weak link. In our best JJ arrays, we obtained average transmission close to unity, e.g., $\bar{\tau} = 0.94$ in reference [43]. If $\bar{\tau}$ is found (and thus the low temperature limit of the CPR), I_0 can then be calculated from $L(0) = \Phi_0/[2\pi I_0 f'(0)]$.

The characterization of $\Delta^*(T)$ requires, instead, data at finite temperature, as it is evident from equation (4). It is important to notice that for an epitaxial Al/InAs 2DEG bilayer, the temperature dependence of the induced gap $\Delta^*(T)$ differs from that predicted by BCS [47–50]. More precisely $\Delta^*(T)$ depends on both the BCS-like gap of the Al film and on the coupling coefficient γ_B between Al film and 2DEG (see, e.g., equation (17) in reference [48] or equation (S7) in reference [43]) which can be determined by fit. However, in the low temperature limit this dependence on γ_B is weak, therefore the extracted $\Delta^*(0) = 130\mu$eV value is independent of theory. In fact, when plugged into equation (5) it provides a number of channels very close to that extracted from the Sharvin resistance [43].

The robust determination of the number of transverse channels in a 3.15 μm-wide conductor allows us to deduce the Fermi wavelength $\lambda_F = 33$ nm. To extract the Fermi velocity, an estimate for the effective mass is needed. For bulk InAs the best estimate [51] is $m^* = 0.026m_0$, where m_0 is the electron mass. In quantum wells, owing to confinement, the effective mass is renormalized [52–54]. In quantum wells with similar layer composition, but with narrower quantum well (4 nm as opposed to 7 nm in our structures), the effective mass was measured to be $m^* = 0.04m_0$ [54]. Since in our wafers the confinement is less pronounced, we expect the effective mass to be in between $0.026m_0$ (bulk InAs) and $0.04m_0$ (reference [54]), i.e., a value near $m^* = 0.03m_0$. With this assumption, we deduce a Fermi velocity $v_\mathrm{F} = 7.31 \times 10^5$ m s^{-1}. The Fermi velocity, together with Al superconducting gap ($\Delta_\mathrm{Al} = 220\mu$eV [43]), allows us to estimate an important parameter for SNS junctions, namely, $\lambda = \mathscr{L}\Delta_\mathrm{Al}/(\hbar v_\mathrm{F}) = 0.046$, where $\mathscr{L} = 100$ nm is the junction length [55]. The fact that λ is so much smaller than unity implies that our junctions can be considered to be deeply in the short junction limit. It allows us to discriminate the above mentioned renormalization of the effective gap [50] from the simple reduction of the ABS-energy because of a non-vanishing length of the junction.

4. SNS junctions with strong spin–orbit coupling: φ_0 and supercurrent diode effect

In this section we will discuss the consequences of the ballistic character on the physics of JJs in the presence of large SOI. Several recent works [9–12] have demonstrated that, in the presence of Rashba SOI and broken time-reversal symmetry, a JJ might show an anomalous Josephson effect, i.e., a φ_0 shift of the CPR. In multimode conductors, the φ_0 shift is mainly determined by the channels with low Fermi velocity.

In a φ_0-junction, a purely sinusoidal CPR is still antisymmetric around the (φ_0-shifted) zero current point, i.e., if $\phi \equiv \varphi - \varphi_0$, then $I(\phi) = -I(-\phi)$. Thus, the positive and negative branch of the CPR are equal and opposite, and the CPR inflection point still occurs at $I = 0$. In our experiments, we show that if the junction is ballistic and an in-plane field is applied perpendicular to the supercurrent direction, then SOI will not simply lead to a φ_0 shift, but will effectively distort the CPR in an asymmetric way, so that positive and negative branches will differ. As a consequence, positive and negative critical currents will differ, giving rise to the supercurrent diode effect.

In the experiments reported in reference [27], we show that the main effect of an in-plane field perpendicular to the current consists in the addition of a cosine term to the CPR, which only contains sine terms in the absence of the magnetic field. If the unperturbed CPR is purely sinusoidal (low $\overline{\tau}$ limit), the addition of a cosine produces a shifted sine, i.e., a phase shift φ_0. However, if higher harmonics in the CPR are not negligible, the situation is more complex. Let us consider first the Fourier expansion of a generic skewed CPR

$$I(\varphi) = \sum_n b_n \sin(n\varphi). \qquad (6)$$

In the presence of magnetic field (and thus anomalous Josephson effect) each n-term would acquire its own $\varphi_{0,n}$ shift. The determination of each $\varphi_{0,n}$ is nontrivial [6], and in general $\varphi_{0,n} \neq n\varphi_0$, where φ_0 is some common phase shift. Therefore, the resulting CPRs will not be merely shifted. Instead, each $\varphi_{0,n}$ shift will be equivalent to the addition of a $a_n \cos(n\varphi)$ term in the Fourier series. In the Furusaki–Beenakker CPR, the Fourier coefficients b_n are exponentially suppressed with n (see supplementary information in reference [27]), therefore, in a rough approximation, only the first terms will be important. Keeping only the leading terms in the approximation

$$I(\varphi) \approx b_1 \sin(\varphi) + a_1 \cos(\varphi) + b_2 \sin(2\varphi), \qquad (7)$$

where a_1 is proportional to both magnetic field and Rashba SOI strength, while b_2 mainly determine the skewedness. The MCA effect requires both a_1 and b_2 to be nonzero, while the simple anomalous shift φ_0 only requires the former.

The supercurrent diode effect can be measured with standard DC transport experiments. Figure 2(a) shows the Fraunhofer pattern measured in sample 1 in the presence of an in-plane field ($B_x = 100$ mT) directed parallel to the supercurrent direction. For this field alignment there is no MCA effect: positive and negative critical currents are the same, i.e., the graph is symmetric around the abscissa axis. In contrast, in the presence of an in-plane field $B_\mathrm{ip} = 75$ mT perpendicular to the current, the critical currents for opposite polarities are different, see figure 2(b). We stress that critical current values in both figures 2(a) and (b) were obtained by sweeping the current from zero to finite (either positive or negative) bias. Interestingly, when the supercurrent diode effect is enabled [figure 2(b)], the critical current difference is pronounced only for small values of B_z, as visible in figure 2(c): this figure shows (symbols) the absolute value of the critical current difference as a function of B_z, normalized to the $B_z = 0$ value. We notice also that such difference oscillates with B_z with a flux period of $\Phi_0/2$, as it can be seen in the zoomed graph in figure 2(d). The peculiar B_z dependence can be captured by the product of the critical current and the first higher harmonic Fourier coefficient b_2 of the Fourier expansion of the Furusaki–Beenakker CPR. The former term contains the envelope of all the harmonics producing the Fraunhofer pattern, while the latter contains the most relevant term for the skewedness of the CPR, which as explained above, determines the diode effect. The curve, calculated from equation (4) with parameters extracted from the experiment [27, 43] [solid line in figure 2(d)] nicely matches the experimental data, including the alternating sequence of cusp-like and quadratic minima. This clearly demonstrates that in short-ballistic JJs the diode effect is mainly determined by the first higher harmonic b_2 above the fundamental term.

Finally, for $B_z = 0$ we can extract the B_ip dependence of the diode effect, depicted in figure 2(e). Up to about $B_\mathrm{ip} \approx 80$ mT, the dependence is nearly linear, as expected by a magnetochiral effect, see equation (1). Above this threshold, the critical current asymmetry rapidly decreases, indicating that pair-breaking is at work. Interestingly, the diode effect is more fragile than bare superconductivity, since it relies on higher harmonics of the CPR, which are suppressed well before the fundamental term. Thus, at sufficiently high field, one still observes finite critical current but no supercurrent diode effect.

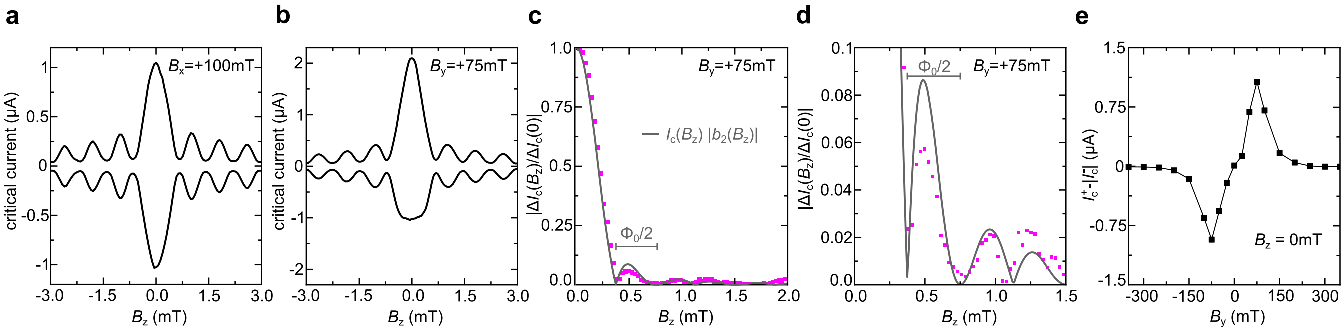

Figure 2. (a) Fraunhofer pattern for sample 1, measured applying an in plane field $B_{\text{ip}} = 100$ mT *parallel* to the current direction. (b) The same measurement for $B_{\text{ip}} = 75$ mT applied *perpendicular* to the current direction. (c) Measured (at $B_{\text{ip}} = 75$ mT) absolute value of the difference $|\Delta I_c|$ between the critical currents for positive and negative bias (symbols), and calculated product $I_c \cdot b_2$ of critical current and second Fourier coefficient (gray line). Both curves are plotted as a function of the out-of-plane field B_z and normalized to the $B_z = 0$ value. (d) Zoom-in that highlights the oscillations of the critical current difference with flux period $\Phi_0/2$. (e) ΔI_c versus B_{ip} at $B_z = 0$.

5. Impact of lattice orientation on magnetochiral anisotropy

As discussed above, the supercurrent diode effect is a direct consequence of the distortion of a skewed CPR produced by an in-plane field in the presence of a spin-split conduction band. The asymmetry between the positive and negative CPR branches implies that (i) positive and negative critical currents are different, (ii) the inductance is not an even function of I anymore, owing to the magnetochiral correction term linear in both current and field, see equation (1). The inductance is proportional to the derivative of the inverse CPR, $\varphi(I)$, therefore (ii) is equivalent to a shift of the CPR inflection point from $I = 0$ to a finite value $I = i^*$. The latter value can be experimentally determined from the minimum of the $L(I)$curve.

In our junctions the MCA is a small correction, therefore we can approximate the $L(I)$ curve as a parabola near zero current, i.e., $L(I) \approx L_0 + L_0' I + L_0'' I^2$. The CPR can then be characterized by the three coefficients L_0,L_0', and L_0''. In particular, it is L_0' that mostly determines the MCA. At finite in-plane field B_{ip}, one can extract the MCA coefficient $\gamma_L \equiv -2L_0'/(L_0 B_{\text{ip}})$. As shown in the $L(I)$ measurements plotted in figure 2 of reference [27], our experiments confirm that it is indeed the in-plane field component perpendicular to the current that determines the MCA. In fact, if the sample is rotated keeping constant the in-plane field magnitude and direction, then both L_0' and γ_L display a sinusoidal dependence on the angle between $\vec{I}$ and $\vec{B}_{\text{ip}}$, with the maximum anisotropy occurring for $\theta = \pm 90°$.

For a conductor with purely Rashba SOI, the direction of the current with respect to the underlying lattice is unimportant, since both spin-split Fermi surfaces are isotropic. For generic Rashba (α) and Dresselhaus (β) SOI parameters, the spin–orbit field $\vec{\Omega}$ is defined such that the perturbative SOI term of the Hamiltonian is [56]

$$H_{\text{SOI}} = \vec{\Omega} \cdot \hat{\vec{\sigma}} = (\alpha - \beta) k_y \hat{\sigma}_x - (\alpha + \beta) k_x \hat{\sigma}_y. \tag{8}$$

The magnitude of the MCA effect depends on the $\vec{\Omega}$ component parallel to the current, corresponding to a k-space direction *perpendicular* to the current [k_y direction for our axis choice, see figures 3(e) and (f)]. In the pure Rashba SOI case ($\beta = 0$), the modulus of the pseudo-magnetic field $|\vec{\Omega}|$ is isotropic (its magnitude does not depend on the direction in the reciprocal space), and thus the particular mutual orientation of current and lattice is irrelevant.

The situation changes in the presence of a small Dresselhaus SOI component ($\beta \neq 0$). In this case, the total spin–orbit field $|\vec{\Omega}|$ is reduced (enhanced) for the k-direction where Rashba and Dresselhaus SOI fields are antiparallel (parallel). As a result, a finite Dresselhaus component breaks the symmetry among different crystal directions. To verify the presence of a Dresselhaus component, we have fabricated an array (sample 3) which is, to the best of our ability, identical to the array used for the measurements reported above (sample 1). The only nominal difference is the orientation of the current with respect to the lattice axes: in sample 1 the current is directed along the [110] direction, while in sample 3 it is directed along the $[1\bar{1}0]$ axis. We have then repeated the inductance MCA measurements, whose results are summarized in figure 3(a). The $L(I)$ curves for different angles θ between $\vec{B}_{\text{ip}}$ and $\vec{I}$ in sample 3 are similar to those for sample 1 reported in reference [27]. Using the same procedure described there, we can extract the L_0,L_0', and L_0'' coefficients; L_0 and L_0' are plotted as a function of θ in figures 3(b) and (c), respectively. The blue (red) curve refers to sample 1 (sample 3). First, we notice that the two L_0 coefficients are very similar (indicating a good reproducibility of the fabrication procedure) and both have a very weak angular dependence [notice the small range for the vertical axis in figure 3(b)]. Second, the L_0' coefficients show small, but important, differences: the amplitude of the 90°–270° excursion is larger in sample 1, while an anomalous plateau near $\theta = 0°$ is more pronounced in sample 3. From those values we can calculate γ_L for the two samples, see figure 3(d). From the amplitude of the quasi-sinusoidal curves, we deduce a ratio r between the maximum L_0' for sample 3 (current parallel to $[1\bar{1}0]$) and that for sample 1 (current parallel to [110]). In our experiment we obtain $r = 0.854$.

As discussed above, $r \neq 1$ can be attributed to a Dresselhaus SOI component. Numerical quantum transport simulations (computed with the KWANT package [57], using the methodology and parameters as described in reference [27])

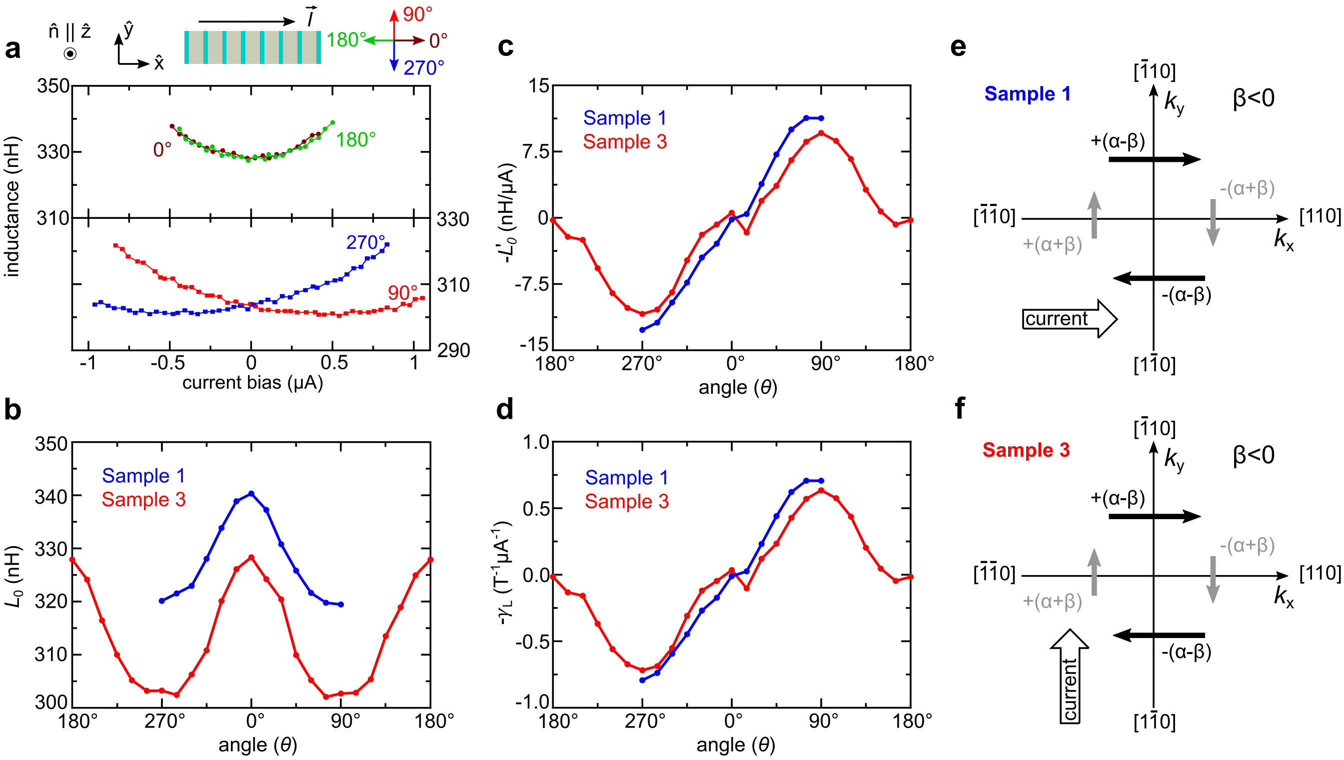

Figure 3. (a) The top sketch shows the mutual orientation of the vectors current $\vec{I}$, in-plane field $\vec{B}_{\mathrm{ip}}$, and $\hat{n}$ (unit vector perpendicular to the surface and pointing to the top) for $\theta = 0°$ (brown), $\theta = 90°$ (red), $\theta = 180°$ (green), and $\theta = 270°$ (blue). The graphs show the $L(I)$ curve for each value of θ, with the same color code. (b) Constant term L_0 (see text) for the measured $L(I)$ curve, plotted as a function of θ for sample 1 (blue) and sample 3 (red). In sample 1 (sample 3) the current is directed along the [110] ([1$\bar{1}$0]) direction. (c) Plot of L_0' as a function of θ for sample 1 and sample 3. (d) Plot of $\gamma_L(\theta)$. (e) Scheme showing the magnitude of the total (Rashba plus Dresselhaus) SOI field in sample 1, sketched for different $\vec{k}$ with respect to the current direction (horizontal). Here we assume $\beta < 0$, which is the case for InAs quantum wells. (f) The same for sample 3. In sample 1 the current direction is directed along the $\vec{k}$ direction where the SOI field is the largest (Rashba and Dresselhaus add), while for sample 3 the current points to the $\vec{k}$ direction of least SOI field.

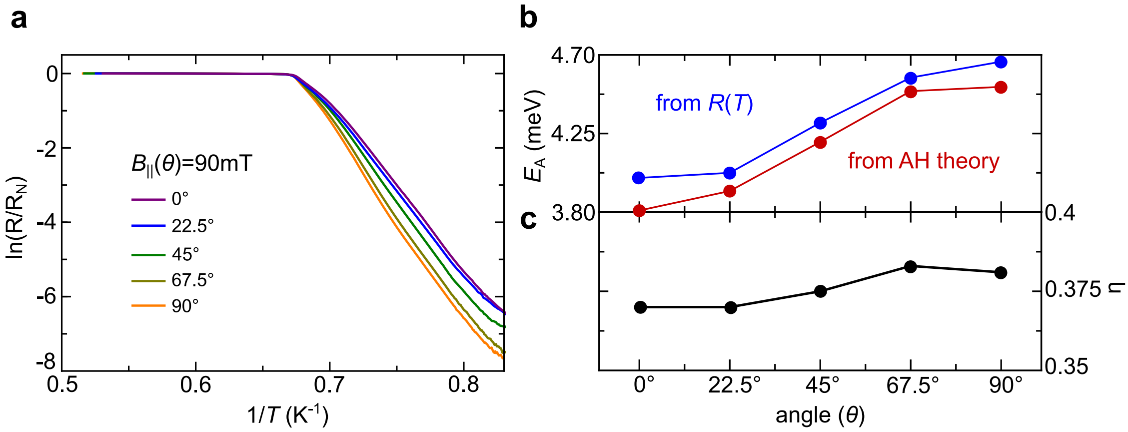

Figure 4. (a) Arrhenius plot of the temperature dependence of the resistance $R(T)$, plotted for different angles θ between current and in-plane magnetic field. (b) Activation energy extracted from the linear part of the graph panel (a) (blue symbols), plotted together with twice the Josephson energy $2E_{\mathrm{J}}$ calculated via the Ambegaokar–Halperin theory (red, see text).

found that in good approximation r is a linear function of $|\beta|$, more precisely $r \approx 1.004 - 0.225|\beta|$ with β expressed in meV nm^{-1} units. On this basis, we can estimate a Dresselhaus parameter of $\beta \approx -0.67$ meV nm^{-1}, which is approximately in line with the $\vec{k}\cdot\vec{p}$ estimate reported in the supplementary information of reference [27].

6. Angle dependence of the thermal activation for phase slips

In the previous sections we have discussed in detail the two-fold anisotropy induced by the in-plane field on L_0', and thus on the inflection point of the CPR, which is at the basis of MCA.

We have also highlighted a weaker, but still evident anisotropy in L_0. A two-fold anisotropy in L_0 is expected to produce a similar anisotropy in the Josephson coupling $E_J = \hbar I_c/2e$ and, consequently, an anisotropic activation energy for phase slips in the junctions.

The experiments discussed so far mainly focus on the deep superconducting regime at temperatures close to the base temperature of our dilution refrigerator, where $T \ll \Delta^*/k_B$. For our JJ arrays the Josephson energy is much larger than the charging energy, thus in this regime we cannot detect any resistive phase slip effect. To investigate the angle dependence of the phase slip rate, we must work in a temperature regime closer to T_c. However, one must keep in mind that sample resistances larger than few ohms are not compatible with the resonator technique. The resonator can indeed be used to measure very small resistance changes via the Q factor, but as long as the total resistance of the RLC tank is above few ohms (roughly 1 mΩ per junction), the resonance is suppressed altogether. Hence, we studied phase slip rates by conventional DC transport measurements.

Figure 4(a) shows the Arrhenius plot of the temperature-dependent resistance near T_c in an in-plane field of 90 mT. Each curve refers to a different angle θ between in-plane field $\vec{B}_{ip}$ and current $\vec{I}$. The resistance is clearly thermally activated with an activation energy that depends on the angle of the in-plane field. At the lowest temperature, there are deviations from the Arrhenius law, most probably due to 2–3 junctions with reduced I_c. From the linear part of the Arrhenius curve we can extract the activation energy, which is plotted versus θ in figure 4(b) (blue symbols). In the same curve (red symbols), we show the corresponding values of twice the Josephson energy, $2E_J$, calculated via the Ambegaokar–Halperin theory [58], adapted to describe junctions with the non-sinusoidal CPR as in equation (4). In the calculation, we could only match (approximately, as seen in panel (b)) the experimental values by multiplying by a factor η the Δ^* expected from equation (17) in reference [48], with parameter $\bar{\tau}$, Δ_{Al} and γ_B extracted from the experiments on sample 3. As shown in figure 4(c) the parameter η is relatively angle independent and close to 0.37, indicating that close to T_c the induced gap is about one third of what expected by equation (17) of reference [48]. On the one hand, this temperature regime is well above that explored in references [27, 43]. On the other, the theory in reference [48] is only valid far from T_c, therefore it does not apply to the measurements in figure 4(a). We have also tried to introduce a certain Gaussian spread of the E_J values in our model. However, even admitting a relatively large spread (standard deviation 25% of the mean value), it is impossible to match the experimental data without a substantial reduction of Δ^* compared to the prediction of equation (17) in reference [48].

7. Conclusions

In conclusion, we have studied the supercurrent diode effect and the MCA for the inductance in arrays of JJs with large spin–orbit coupling. These experiments complement those reported in the literature. We observe a dependence of the diode effect on the mutual orientation of supercurrent and lattice axes, which signals the presence of an additional Dresselhaus spin–orbit coupling term. Finally, we can correlate the anisotropy in the in-plane field dependence of the inductance with that of the phase-slip activation energy obtained from standard DC transport measurements. Superconducting diodes are the first step towards dissipation-free electronics. In perspective, they might play a crucial role in dissipationless memories, or in superconducting microwave detectors with ultra-high sensitivity.

Acknowledgments

We thank Hugues Pothier for helpful discussion. CB, LF, AC, SR, PEFJ, DK, JF, NP, CS acknowledge funding by the Deutsche Forschungsgemeinschaft (DFG, German Research Foundation)—Project-ID 314695032—SFB 1277 (Subprojects B05, B07, and B08). AC, PEFJ, DK, JF also benefited from the European Union's Horizon 2020 research and innovation programme under Grant Agreement No. 881603 (Graphene Flagship Core 3). AC and JF also acknowledge support from the DFG Project 454646522. Work completed by SG, GCG, TL, MJM is supported by Microsoft Quantum.

Data availability statement

The data that support the findings of this study are available upon reasonable request from the authors.

ORCID iDs

A Costa https://orcid.org/0000-0001-5706-2198
Jordi Picó-Cortés https://orcid.org/0000-0002-7705-3966
S Reinhardt https://orcid.org/0000-0002-5266-7355
G C Gardner https://orcid.org/0000-0001-5469-9257
M J Manfra https://orcid.org/0000-0002-2049-8438
P E Faria Junior https://orcid.org/0000-0002-1161-2059
D Kochan https://orcid.org/0000-0003-0613-5996
J Fabian https://orcid.org/0000-0002-3009-4525
N Paradiso https://orcid.org/0000-0002-1797-2901
C Strunk https://orcid.org/0000-0001-9982-0022

References

[1] Golubov A A, Kupriyanov M Y and Il'ichev E 2004 The current–phase relation in Josephson junctions *Rev. Mod. Phys.* **76** 411
[2] Bezuglyi E V, Rozhavsky A S, Vagner I D and Wyder P 2002 Combined effect of Zeeman splitting and spin–orbit interaction on the Josephson current in a superconductor—two-dimensional electron gas–superconductor structure *Phys. Rev.* B **66** 052508
[3] Buzdin A 2008 Direct coupling between magnetism and superconducting current in the Josephson φ_0 junction *Phys. Rev. Lett.* **101** 107005

[4] Reynoso A A, Usaj G, Balseiro C A, Feinberg D and Avignon M 2008 Anomalous Josephson current in junctions with spin polarizing quantum point contacts *Phys. Rev. Lett.* **101** 107001
[5] Reynoso A A, Usaj G, Balseiro C A, Feinberg D and Avignon M 2012 Spin–orbit-induced chirality of Andreev states in Josephson junctions *Phys. Rev.* B **86** 214519
[6] Yokoyama T, Eto M and Nazarov Y V 2014 Anomalous Josephson effect induced by spin–orbit interaction and Zeeman effect in semiconductor nanowires *Phys. Rev.* B **89** 195407
[7] Shen K, Vignale G and Raimondi R 2014 Microscopic theory of the inverse Edelstein effect *Phys. Rev. Lett.* **112** 096601
[8] Konschelle F, Tokatly I V and Bergeret F S 2015 Theory of the spin-galvanic effect and the anomalous phase shift φ_0 in superconductors and Josephson junctions with intrinsic spin–orbit coupling *Phys. Rev.* B **92** 125443
[9] Szombati D B, Nadj-Perge S, Car D, Plissard S R, Bakkers E P A M and Kouwenhoven L P 2016 Josephson φ_0-junction in nanowire quantum dots *Nat. Phys.* **12** 568
[10] Assouline A *et al* 2019 Spin–orbit induced phase-shift in Bi_2Se_3 Josephson junctions *Nat. Commun.* **10** 126
[11] Mayer W, Dartiailh M C, Yuan J, Wickramasinghe K S, Rossi E and Shabani J 2020 Gate controlled anomalous phase shift in Al/InAs Josephson junctions *Nat. Commun.* **11** 212
[12] Strambini E *et al* 2020 A Josephson phase battery *Nat. Nanotechnol.* **15** 656
[13] Rikken G L J A, Fölling J and Wyder P 2001 Electrical magnetochiral anisotropy *Phys. Rev. Lett.* **87** 236602
[14] Rikken G L J A and Wyder P 2005 Magnetoelectric anisotropy in diffusive transport *Phys. Rev. Lett.* **94** 016601
[15] Rikken G L J A and Avarvari N 2019 Strong electrical magnetochiral anisotropy in tellurium *Phys. Rev.* B **99** 245153
[16] Legg H F *et al* 2021 Giant magnetochiral anisotropy from quantum confined surface states of topological insulator nanowires (arXiv:2109.05188 [cond-mat.mes-hall])
[17] Meng K K, Chen J K, Miao J, Xu X G and Jiang Y 2021 Interface-driven electrical magnetochiral anisotropy in Pt/PtMnGa bilayers *Appl. Phys. Lett.* **118** 252403
[18] Morimoto T and Nagaosa N 2016 Chiral anomaly and giant magnetochiral anisotropy in noncentrosymmetric Weyl semimetals *Phys. Rev. Lett.* **117** 146603
[19] Wang Y, Legg H F, Boemerich T, Park J, Biesenkamp S, Taskin A A, Braden M, Rosch A and Ando Y 2021 Gigantic magnetochiral anisotropy in the topological semimetal $ZrTe_5$ (arXiv:2011.03329 [cond-mat.mes-hall])
[20] Hoshino S, Wakatsuki R, Hamamoto K and Nagaosa N 2018 Nonreciprocal charge transport in two-dimensional noncentrosymmetric superconductors *Phys. Rev.* B **98** 054510
[21] Tokura Y and Nagaosa N 2018 Nonreciprocal responses from non-centrosymmetric quantum materials *Nat. Commun.* **9** 3740
[22] Wakatsuki R, Saito Y, Hoshino S, Itahashi Y M, Ideue T, Ezawa M, Iwasa Y and Nagaosa N 2017 Nonreciprocal charge transport in noncentrosymmetric superconductors *Sci. Adv.* **3** e1602390
[23] Yasuda K, Yasuda H, Liang T, Yoshimi R, Tsukazaki A, Takahashi K S, Nagaosa N, Kawasaki M and Tokura Y 2019 Nonreciprocal charge transport at topological insulator/superconductor interface *Nat. Commun.* **10** 2734
[24] Itahashi Y M, Ideue T, Saito Y, Shimizu S, Ouchi T, Nojima T and Iwasa Y 2020 Nonreciprocal transport in gate-induced polar superconductor $SrTiO_3$ *Sci. Adv.* **6** eaay9120
[25] Ideue T, Koshikawa S, Namiki H, Sasagawa T and Iwasa Y 2020 Giant nonreciprocal magnetotransport in bulk trigonal superconductor $PbTase_2$ *Phys. Rev. Res.* **2** 042046
[26] Zhang E *et al* 2020 Nonreciprocal superconducting $NbSe_2$ antenna *Nat. Commun.* **11** 5634
[27] Baumgartner C *et al* 2021 Supercurrent rectification and magnetochiral effects in symmetric Josephson junctions *Nat. Nanotechnol.* **17** 39
[28] Hu J, Wu C and Dai X 2007 Proposed design of a Josephson diode *Phys. Rev. Lett.* **99** 067004
[29] Ando F, Miyasaka Y, Li T, Ishizuka J, Arakawa T, Shiota Y, Moriyama T, Yanase Y and Ono T 2020 Observation of superconducting diode effect *Nature* **584** 373
[30] Bauriedl L *et al* 2021 Supercurrent diode effect and magnetochiral anisotropy in few-layer $NbSe_2$ nanowires (arXiv:2110.15752 [cond-mat.supr-con])
[31] Shin J, Son S, Yun J, Park G, Zhang K, Shin Y J, Park J-G and Kim D 2021 Magnetic proximity-induced superconducting diode effect and infinite magnetoresistance in van der Waals heterostructure (arXiv:2111.05627 [cond-mat.supr-con])
[32] He J J, Tanaka Y and Nagaosa N 2021 A phenomenological theory of superconductor diodes in presence of magnetochiral anisotropy (arXiv:2106.03575 [cond-mat.supr-con])
[33] Pal B *et al* 2021 Josephson diode effect from Cooper pair momentum in a topological semimetal (arXiv:2112.11285 [cond-mat.supr-con])
[34] Diez-Merida J *et al* 2021 Magnetic Josephson junctions and superconducting diodes in magic angle twisted bilayer graphene (arXiv:2110.01067 [cond-mat.supr-con])
[35] Lin J-X *et al* 2021 Zero-field superconducting diode effect in twisted trilayer graphene (arXiv:2112.07841 [cond-mat.mes-hall])
[36] Scammell H D, Li J I A and Scheurer M S 2021 Theory of zero-field diode effect in twisted trilayer graphene (arXiv:2112.09115 [cond-mat.mes-hall])
[37] Zinkl B, Hamamoto K and Sigrist M 2021 Symmetry conditions for the superconducting diode effect in chiral superconductors (arXiv:2111.05340 [cond-mat.supr-con])
[38] Davydova M, Prembabu S and Fu L 2021 Universal Josephson diode effect (arXiv:2201.00831 [cond-mat.supr-con])
[39] Zhang Y, Gu Y, Hu J and Jiang K 2021 General theory of Josephson diodes (arXiv:2112.08901 [cond-mat.supr-con])
[40] Halterman K, Alidoust M, Smith R and Starr S 2021 Supercurrent diode effect, spin torques, and robust zero-energy peak in planar half-metallic trilayers (arXiv:2111.01242 [cond-mat.supr-con])
[41] Watanabe H, Daido A and Yanase Y 2021 Nonreciprocal Meissner response in parity-mixed superconductors arXiv:2109.14874
[42] Zhai B, Li B, Wen Y, Wu F and He J 2022 Prediction of ferroelectric superconductors with reversible superconducting diode effect (arXiv:2201.01775 [cond-mat.supr-con])
[43] Baumgartner C, Fuchs L, Frész L, Reinhardt S, Gronin S, Gardner G C, Manfra M J, Paradiso N and Strunk C 2021 Josephson inductance as a probe for highly ballistic semiconductor–superconductor weak links *Phys. Rev. Lett.* **126** 037001
[44] Meservey R and Tedrow P M 1969 Measurements of the kinetic inductance of superconducting linear structures *J. Appl. Phys.* **40** 2028
[45] Furusaki A and Tsukada M 1991 DC Josephson effect and Andreev reflection *Solid State Commun.* **78** 299
[46] Beenakker C W J and van Houten H 1991 Josephson current through a superconducting quantum point contact shorter than the coherence length *Phys. Rev. Lett.* **66** 3056
[47] Chrestin A, Matsuyama T and Merkt U 1997 Evidence for a proximity-induced energy gap in Nb/INAS/Nb junctions *Phys. Rev.* B **55** 8457
[48] Aminov B A, Golubov A A and Kupriyanov M Y 1996 Quasiparticle current in ballistic constrictions with finite transparencies of interfaces *Phys. Rev.* B **53** 365
[49] Schäpers T 2001 *Superconductor/Semiconductor Junctions* (*International Series in Pure and Applied Physics* vol 174) (Berlin: Springer)

[50] Kjaergaard M, Suominen H J, Nowak M P, Akhmerov A R, Shabani J, Palmstrøm C J, Nichele F and Marcus C M 2017 Transparent semiconductor–superconductor interface and induced gap in an epitaxial heterostructure Josephson junction *Phys. Rev. Appl.* **7** 034029
[51] Vurgaftman I, Meyer J R and Ram-Mohan L R 2001 Band parameters for III–V compound semiconductors and their alloys *J. Appl. Phys.* **89** 5815
[52] Yang M J, Lin-Chung P J, Shanabrook B V, Waterman J R, Wagner R J and Moore W J 1993 Enhancement of cyclotron mass in semiconductor quantum wells *Phys. Rev.* B **47** 1691
[53] Pryor C E and Pistol M-E 2005 Band-edge diagrams for strained III–V semiconductor quantum wells, wires, and dots *Phys. Rev.* B **72** 205311
[54] Yuan J *et al* 2020 Experimental measurements of effective mass in near-surface InAs quantum wells *Phys. Rev.* B **101** 205310
[55] Metzger C, Park S, Tosi L, Janvier C, Reynoso A A, Goffman M F, Urbina C, Levy Yeyati A and Pothier H 2021 Circuit-qed with phase-biased Josephson weak links *Phys. Rev. Res.* **3** 013036
[56] Ganichev S D *et al* 2004 Experimental separation of Rashba and Dresselhaus spin splittings in semiconductor quantum wells *Phys. Rev. Lett.* **92** 256601
[57] Groth C W, Wimmer M, Akhmerov A R and Waintal X 2014 KWANT: a software package for quantum transport *New J. Phys.* **16** 063065
[58] Ambegaokar V and Halperin B I 1969 Voltage due to thermal noise in the DC Josephson effect *Phys. Rev. Lett.* **22** 1364